https://doi.org/10.3311/PPci.42956

Periodica Polytechnica Civil Engineering, 70(2), pp. 411–423, 2026

Stress-based Bi-directional Evolutionary Structural Optimization Method with Incremental Nonlinear Structural Analysis

Xianda Chen[1], Huzhi Zhang[1*], Qingchao He[1], Bin Yin[1]

[1] School of Civil Engineering, Hunan University of Science and Technology, Taoyuan Road, Yuhu District, 411201 Xiangtan, China
[*] Corresponding author, e-mail: zhanghz_hnu@163.com

Received: 02 December 2025, Accepted: 01 April 2026, Published online: 22 April 2026

Abstract

To extend the applicability of optimization methods in civil engineering, particularly for structural members incorporating cement-based materials like concrete, this study proposes a stress-based bi-directional evolutionary structural optimization (BESO) framework integrated with incremental nonlinear structural analysis. The core objective is to minimize peak stress in structures by leveraging the *p*-norm function (p = 4–6) to approximate stress concentration and sensitivity numbers derived *via* the adjoint method. The proposed approach is validated for optimizing structures with highly nonlinear material behaviors. By tuning the *p*-value (4–6) during optimization, solutions aligned with predetermined objectives are achieved through element sensitivity analysis. The sensitivity numbers are computed by filtering initial values derived from incremental nonlinear stress analysis results. Subsequent sensitivity filtering and iterative design variable updates ensure convergence to stable solutions matching the optimization goals. The method incorporates von Mises stress for nonlinear material modeling and addresses numerical challenges like mesh dependency through dual filtering strategies as verified by two-dimensional/three-dimensional examples including irregular beams and cantilever structures. This framework provides a robust tool for topology optimization of civil structures with strongly nonlinear materials, balancing accuracy and computational efficiency under volume constraints.

Keywords

topology optimization, BESO, peak stress, material nonlinearity, incremental nonlinear structural analysis

1 Introduction

Topology optimization [1, 2], a mathematical approach for determining optimal material distribution, has developed into an advanced conceptual design method [3] in recent decades. Its application has expanded across diverse fields, including aerospace [4], mechanical engineering [5], bridge engineering [6], and building engineering [7, 8].

Early topology optimization methods primarily focused on frequency [9, 10] and stiffness [11] under volume constraints, limiting their applicability to strength-based engineering designs. To address this gap, stress-based topology optimization approaches were developed. Nevertheless, three persistent challenges have hindered progress: the "singularity" issue, stress localization, and highly nonlinear material behaviors [12].

Recent advancements in stress-based topology optimization have introduced innovative approaches, including the ε-relaxation method [13, 14] for singularity avoidance, the *qp*-relaxation method [15, 16] for stress constraints, the bi-directional evolutionary structural optimization (BESO) method [17, 18] for discrete optimization, and global aggregation techniques such as *p*-norm functions [19] and the Kresselmeier-Steinhauser function [20]. Additionally, design variable filtering and updating strategies [18, 21] were proposed to mitigate inherent challenges in stress-based topology optimization approaches. These advancements have significantly advanced the field, enabling applications in lightweight design [22] and balancing structural strength with stiffness [23]. Notably, recent studies have extended stress-based topology optimization to incorporate elasto-plastic and plastic-limit behaviors under nonlinear material conditions [24, 25], further enriching the method's applicability to complex engineering scenarios.

Recent studies have adopted B-spline and non-uniform rational B-spline (NURBS) representations to advance topology optimization, moving beyond traditional methods limited to linear-elastic materials. Notably, Izzi et al. [26]

Cite this article as: Chen, X., Zhang, H., He, Q., Yin, B. "Stress-based Bi-directional Evolutionary Structural Optimization Method with Incremental Nonlinear Structural Analysis", Periodica Polytechnica Civil Engineering, 70(2), pp. 411–423, 2026. https://doi.org/10.3311/PPci.42956

developed a theoretical framework for optimizing variable-stiffness composite laminates under strength and mass constraints. Montemurro and Roiné [27] proposed a strength-based topology optimization method using NURBS hyper-surfaces to model pseudo-density fields. Roiné et al. [28] introduced the solid isotropic material with penalization algorithm incorporating NURBS hyper-surfaces for stress control in continuum topology optimization.

Early research in structural optimization considered material and geometric nonlinearities. Key contributions include direct differentiation and adjoint variable methods [29, 30] for nonlinear sensitivity analysis. These methods, albeit computationally demanding, provide a rigorous foundation for accurate nonlinear optimization. Applications include crashworthiness design of transient frame structures [31] and linear/nonlinear plate analysis [32]. Subsequent developments included displacement-loaded nonlinear optimization [33, 34], dual algorithms for local stress constraints [35], stress-constrained nonlinear optimization [23], and sensitivity filter radius reduction strategies [36], all of which expanded application domains and improved stability.

In such optimization, the accuracy of nonlinear structural analysis directly impacts results. Xu et al. [37] addressed this by developing an incremental BESO method incorporating load steps, achieving notable improvements in peak and global stress control. However, this approach calculates sensitivity numbers solely from the final load step, neglecting sensitivity superposition across load steps and reducing accuracy. Conversely, Han et al. [38] integrated quasi-static nonlocal damage models with finite-element analysis (FEA) to model progressive damage and developed a stress-based topology optimization method considering nonlinear continuous damage. Accounting for element damage accumulation in each load step, their method neglects unbalanced force effects, limiting its effectiveness to structures with weak nonlinearity.

For structures with strongly nonlinear materials like civil engineering cement-based composites, stress-strain relationships are path-dependent, and strain cannot be uniquely determined by stress alone. During elastoplastic deformation, the strain state depends on both the current stress state and the stress history. Simplified nonlinear analysis methods thus introduce significant errors in stress calculations, complicating the attainment of optimal structural designs. Thus, for civil engineering structures with cement-based materials like concrete, accurately accounting for unbalanced force effects on stiffness matrices in each load step of incremental nonlinear analysis – and using high-precision stress calculations to construct sensitivity information – is essential for integrating stress-based topology optimization into designs with strongly nonlinear materials.

This work advances nonlinear stress-based BESO *via* fundamental innovations, with core novelties in three integrated aspects: sensitivity accumulation across all load increments (linking cement-based materials' path-dependent behavior to sensitivity quantification, unlike existing incremental BESO ignoring multi-step superposition), a revised adjoint formulation embedding unbalanced force evolution constraints (addressing damage-based methods' neglect of unbalanced force effects on stiffness matrices), and a dual-filtering strategy tailored for aggregated nonlinear sensitivities (mitigating numerical instabilities in strongly nonlinear topology optimization, distinct from generic filtering in linear/weakly nonlinear methods). Additionally, *p*-norm peak stress approximation is rigorously integrated with incremental nonlinear equilibrium conditions.

This paper, therefore, proposes applying the BESO method to structures with strongly nonlinear materials, leveraging stress results from incremental nonlinear FEA. It is organized as follows:

- Section 2 introduces the stress-based BESO method with incremental nonlinear structural analysis, including the establishment of peak stress optimization objectives and element sensitivity construction/filtering;
- Section 3 presents the optimization process and verifies effectiveness *via* a two-dimensional (2D) example;
- Section 4 confirms applicability through traditional structure optimization;
- Section 5 compares with existing linear-elastic stress-based methods using a 2D example;
- Section 6 validates generality *via* a three-dimensional (3D) example;
- Section 7 discusses the impact of the *p*-value;
- Section 8 contains the conclusions of our article.

2 Stress-based BESO method

2.1 Optimization objective

Considering material nonlinearity, the mathematical model for minimizing the peak stress of the structure based on volume constraints can be described as follows:

$$\begin{aligned} &\text{find: } \boldsymbol{x} = \left[x_1, x_2, \ldots, x_i, \ldots, x_n\right] \quad \left(x_i = 0 \text{ or } 1\right) \\ &\text{minimize: } f\left(\boldsymbol{x}\right) = \sigma^{\max} \\ &= \max\left(\sigma_{vm,1}, \sigma_{vm,2}, \ldots, \sigma_{vm,i}, \ldots, \sigma_{vm,n}\right) \\ &\text{subject to: } \boldsymbol{R}\left(\boldsymbol{U}, \boldsymbol{x}\right) = \boldsymbol{0} \\ &\qquad V\left(\boldsymbol{x}\right) = \sum x_i v_i = V_{req} \end{aligned} \quad , \tag{1}$$

where $\sigma^{\max}$ represents the maximum stress in the structure, and $\sigma v_{m,i}$ denotes the equivalent stress at the centroid of the i-element. V and V_{req} respectively denote the current volume and the target volume of materials. v_i denotes the volume of element i. The vector $\boldsymbol{x}$ is the design variable vector, signifying the determination of a set of solution vectors to minimize the objective function $f(\boldsymbol{x})$. Meanwhile, x_i represents the design variable of element i, with a value of 0 or 1, corresponding to the removal and retention status of the element. Finally, $\boldsymbol{R}$ denotes the unbalanced force in the structure. In the structural FEA for optimization, reinforced concrete is modeled as a composite material with tensile and compressive strength. Although this process may introduce minor deviations, the optimization retains sufficient accuracy for guiding conceptual design. Thus, the equivalent stress (i.e., von Mises stress) is adopted as the stress measure for optimization. It is acknowledged that this involves a simplification for reinforced concrete, as the von Mises criterion does not capture the material's tension-compression asymmetry. While acceptable for conceptual design where global load paths are the primary concern, this may underestimate the criticality of tensile regions, potentially leading to unconservative topologies for tension-dominated failure modes. Future work could extend the framework to orthotropic or pressure-dependent criteria to better reflect concrete behavior.

Assuming that the material constitutive relations are independent of the design variable x_i, the calculation of the equivalent stress at the centroid of the element is performed to the following formula:

$$\begin{aligned}\sigma_{vm} &= \left\{\left[\begin{array}{l}\left(\sigma_x-\sigma_y\right)^2+\left(\sigma_y-\sigma_z\right)^2\\ +\left(\sigma_z-\sigma_x\right)^2+6\left(\tau_{xy}^2+\tau_{yz}^2+\tau_{zx}^2\right)\end{array}\right]\Big/2\right\}^{\frac{1}{2}}\\ &=\left(\boldsymbol{\sigma}^T\boldsymbol{V}\boldsymbol{\sigma}\right)^{\frac{1}{2}},\end{aligned} \tag{2}$$

where σ_x, σ_y and σ_z represent the components of stress in the x-direction, y-direction and z-direction, respectively. τ_{xy}, τ_{yz} and τ_{zx} denote the components of the shear stress. $\boldsymbol{\sigma}$ is a stress vector following the Voigt rule, and $\boldsymbol{V}$ is the stress coefficient matrix employed to compute the equivalent stress. For the 2D plane stress problem, the expression of $\boldsymbol{V}$ is given in Eq. (3), while for the 3D problem, it is given in Eq. (4), respectively.

$$\boldsymbol{V}=\begin{bmatrix}1 & -0.5 & 0\\ -0.5 & 1 & 0\\ 0 & 0 & 3\end{bmatrix} \tag{3}$$

$$\boldsymbol{V}=\begin{bmatrix}1 & -0.5 & -0.5 & 0 & 0 & 0\\ -0.5 & 1 & -0.5 & 0 & 0 & 0\\ -0.5 & -0.5 & 1 & 0 & 0 & 0\\ 0 & 0 & 0 & 3 & 0 & 0\\ 0 & 0 & 0 & 0 & 3 & 0\\ 0 & 0 & 0 & 0 & 0 & 0\end{bmatrix} \tag{4}$$

Given the local nature of stress and the inherent discontinuity of the maximum function, the p-norm function [18] is employed to approximate peak stress. The specific formulation of the p-norm function is expressed as:

$$\text{minimze: } \sigma_{PN}=\left(\sum_{i=1}^{n}\sigma_{vm,i}^{p}\right)^{1/p}\approx f\left(\boldsymbol{x}\right), \tag{5}$$

where σ_{PN} represents the p-norm stress aggregation function, and p is the stress norm parameter that requires manual adjustment. When the p-value is set to 1, σ_{PN} equals to the sum of stress. As the p-value increases, σ_{PN} approaches $\sigma^{\max}$; on the contrary, the p-norm problem becomes ill-conditioned [18]. The selection of the pre-specified p-value warrants further investigation.

2.2 Optimization sensitivity

The adjoint method [19] is employed to derive sensitivity numbers. This requires establishing the relationship between design variables and element stiffness, which is first approximated linearly as:

$$\boldsymbol{D}_i=x_i\boldsymbol{D}_0, \tag{6}$$

where $\boldsymbol{D}_i$ and $\boldsymbol{D}_0$ denote the effective stiffness matrix of element i during FEA and the stiffness matrix of the solid materials, respectively.

Consider the effective stress vector of element i as follows:

$$\boldsymbol{\sigma}_i=\boldsymbol{D}_i\boldsymbol{B}_i\boldsymbol{u}_i/x_i=\boldsymbol{D}_0\boldsymbol{B}_i\boldsymbol{u}_i, \tag{7}$$

where $\boldsymbol{\sigma}_i$ and $\boldsymbol{u}_i$ denote the stress vector and displacement vector of element i, respectively. $\boldsymbol{B}_i$ denotes the strain-displacement matrix. Under the small deformation assumption adopted in this study, the strain-displacement matrix $\boldsymbol{B}$ remains invariant to design variables. To avoid re-meshing and global stiffness matrix singularity, an extremely low stiffness is assigned to void regions in practice.

The structurally unbalanced force $\boldsymbol{R}$ in the constraint conditions of Eq. (1) can be calculated as follows:

$$\boldsymbol{R}\left(\boldsymbol{U},\boldsymbol{x}\right)=\boldsymbol{F}-\sum_{i=1}^{n}x_i\int_{\Omega_i}\boldsymbol{B}_i^T\boldsymbol{\sigma}_i d\Omega_i=\boldsymbol{0}, \tag{8}$$

where $\boldsymbol{F}$ denotes the force vector. Herein, Newton Raphson's method is employed to solve nonlinear equilibrium equations. The 2-norm is adopted to quantify the structural unbalanced force. When this value falls below the predefined threshold (set to 10 throughout this study), the nonlinear FEA results are deemed sufficiently accurate and converged.

In FEA, the unbalanced force at each load step equals zero. Therefore, the formula for calculating the difference $\Delta \boldsymbol{R}_k$ between the unbalanced force at the k-th load step and its previous load step (the (k−1)-th load step) is as follows:

$$\Delta \boldsymbol{R}_k = \boldsymbol{R}_k - \boldsymbol{R}_{k-1} = \Delta \boldsymbol{F}_k - \sum_{i=1}^{n} x_i \int_{\Omega_i} \boldsymbol{L}_i \boldsymbol{B}_i^T \Delta \boldsymbol{\sigma}_{ik} d\Omega_i = \boldsymbol{0}, \tag{9}$$

where $\boldsymbol{L}_i$ is an index matrix employed to index local matrices from the global matrix, such as the nodal displacement vector $\boldsymbol{u}_i = \boldsymbol{L}_i \boldsymbol{U}$ and the nodal force vector $\boldsymbol{f}_i = \boldsymbol{L}_i \boldsymbol{F}$. By substituting Eq. (7) into Eq. (9) and differentiating Eq. (9) with respect to the design variable x_j yields:

$$\begin{aligned}
\frac{\partial \Delta \boldsymbol{R}_k}{\partial x_j} &= \frac{\partial \Delta \boldsymbol{F}_k}{\partial x_j} - \int_{\Omega_j} \boldsymbol{L}_i \boldsymbol{B}_j^T \Delta \boldsymbol{\sigma}_{jk} d\Omega_j - \sum_{i=1}^{n} x_i \boldsymbol{L}_i \boldsymbol{B}_i^T \frac{\partial \Delta \boldsymbol{\sigma}_{ik}}{\partial x_j} \\
&= \frac{\partial \Delta \boldsymbol{F}_k}{\partial x_j} - \int_{\Omega_j} \boldsymbol{L}_i \boldsymbol{B}_j^T \Delta \boldsymbol{\sigma}_{jk} d\Omega_j - \boldsymbol{B}_j^T \boldsymbol{D}_j \boldsymbol{B}_j \boldsymbol{L}_j \frac{\partial \Delta \boldsymbol{u}_{jk}}{\partial x_j} \\
&= \frac{\partial \Delta \boldsymbol{F}_k}{\partial x_j} - \int_{\Omega_j} \boldsymbol{L}_i \boldsymbol{B}_j^T \Delta \boldsymbol{\sigma}_{jk} d\Omega_j - \boldsymbol{K}_k^t \frac{\partial \Delta \boldsymbol{U}_k}{\partial x_j}
\end{aligned}, \tag{10}$$

where $\boldsymbol{K}_k^t$ represents the tangent global stiffness matrix of the nonlinear system at the k-th load increment-step equilibrium.

In the BESO method, the traditional method for considering constraints other than volume constraints is to introduce Lagrange multipliers to augment the design objectives. To enable the computation of sensitivity numbers, a constraint condition $\Delta \boldsymbol{R}_k = \boldsymbol{0}$ is integrated into the objective function through the introduction of a set of Lagrange multiplier vectors denoted as $\boldsymbol{\lambda}_k$:

$$f^*(\boldsymbol{x}) = \sigma_{PN} + \sum_{k=1}^{N} \left(\boldsymbol{\lambda}_k^T \Delta \boldsymbol{R}_k \right), \tag{11}$$

where k represents the k-th load step, and N denotes the total number of load steps in the FEA.

In the analysis of the k-th load step, the approximations are as follows:

$$\Delta \boldsymbol{F}_k = \boldsymbol{K}_k^t \Delta \boldsymbol{U}_k, \tag{12}$$

where $\Delta \boldsymbol{F}_k$ and $\Delta \boldsymbol{U}_k$ denote the load increment matrix and displacement increment matrix at the k-th load step, respectively. $\boldsymbol{K}_k^t = -\partial \boldsymbol{F}_k / \partial \boldsymbol{U}_k$ represents the tangent global stiffness matrix of the nonlinear system at the k-th load increment step equilibrium.

By simultaneously computing the derivative of the design variable x_j on both sides of Eq. (12), the following can be derived:

$$\frac{\partial \boldsymbol{K}_k^t}{\partial x_j} \Delta \boldsymbol{U}_k + \boldsymbol{K}_k^t \frac{\partial \Delta \boldsymbol{U}_k}{\partial x_j} = \boldsymbol{0}. \tag{13}$$

Due to the fact that during force loading, $\partial \Delta \boldsymbol{F}_k / \partial x_j = \boldsymbol{0}$. By taking the derivative of x_j on both sides of Eq. (10) and substituting it into Eq. (11), we can obtain:

$$\begin{aligned}
\frac{\partial f^*(\boldsymbol{x})}{\partial x_j} &= \frac{\partial \sigma_{PN}}{\partial x_j} + \sum_{k=1}^{N} \left(\boldsymbol{\lambda}_k^T \frac{\partial \Delta \boldsymbol{R}_k}{\partial x_j} \right) \\
&= \sigma_{PN}^{1-p} \left(\sum_{i=1}^{n} \sigma_{vm,i}^{p-1} \frac{\partial \sigma_{vm,i}}{\partial \boldsymbol{\sigma}_i} \frac{\partial \boldsymbol{\sigma}_i}{\partial x_j} \right) \\
&+ \sum_{k=1}^{N} \boldsymbol{\lambda}_k^T \left\{ \sum_{i=1}^{n} \left[\frac{\partial \Delta \boldsymbol{F}_k}{\partial x_j} - \int_{\Omega_i} \boldsymbol{L}_i \boldsymbol{B}_i^T \Delta \boldsymbol{\sigma}_{ik} d\Omega_i - \boldsymbol{K}_k^t \frac{\partial \Delta \boldsymbol{U}_k}{\partial x_j} \right] \right\} \\
&= \sum_{k=1}^{N} \left\{ -\sigma_{PN}^{1-p} \sum_{i=1}^{n} \begin{bmatrix} \left(\sigma_{vm,i}^{p-2} \boldsymbol{\sigma}_i^T \boldsymbol{V} \boldsymbol{D}_{ik}^t \boldsymbol{B}_i \boldsymbol{L}_i \right) \left(\boldsymbol{K}_k^t \right)^{-1} \frac{\partial \boldsymbol{K}_k^t}{\partial x_j} \Delta \boldsymbol{U}_k \\ -\boldsymbol{\lambda}_k^T \left(\int_{\Omega_i} \boldsymbol{L}_i \boldsymbol{B}_i^T \Delta \boldsymbol{\sigma}_{ik} d\Omega_i + \boldsymbol{K}_k^t \frac{\partial \Delta \boldsymbol{U}_k}{\partial x_j} \right) \end{bmatrix} \right\}.
\end{aligned} \tag{14}$$

Substituting Eq. (13) into Eq. (14) yields:

$$\frac{\partial f^*(\boldsymbol{x})}{\partial x_j} = \sum_{k=1}^{N} \begin{Bmatrix} \sigma_{PN}^{1-p} \sum_{i=1}^{n} \left(\sigma_{vm,i}^{p-2} \boldsymbol{\sigma}_i^T \boldsymbol{V} \boldsymbol{D}_{ik}^t \boldsymbol{B}_i \boldsymbol{L}_i \right) \frac{\partial \Delta \boldsymbol{U}_k}{\partial x_j} \\ -\boldsymbol{\lambda}_k^T \sum_{i=1}^{n} \left(\int_{\Omega_i} \boldsymbol{L}_i \boldsymbol{B}_i^T \Delta \boldsymbol{\sigma}_{ik} d\Omega_i + \boldsymbol{K}_k^t \frac{\partial \Delta \boldsymbol{U}_k}{\partial x_j} \right) \end{Bmatrix}. \tag{15}$$

According to Eqs. (14) and (15), we can further obtain the derivative of Eq. (11) with respect to x_j as follows in Eq. (16):

$$\begin{aligned}
&\frac{\partial f^*(\boldsymbol{x})}{\partial x_j} \\
&= \frac{1}{2} \sum_{k=1}^{N} \left[\sigma_{PN}^{1-p} \sum_{i=1}^{n} \left(\sigma_{vm,i}^{p-2} \boldsymbol{\sigma}_i^T \boldsymbol{V} \boldsymbol{D}_{ik}^t \boldsymbol{B}_i \boldsymbol{L}_i \right) - 2 \boldsymbol{\lambda}_k^T \boldsymbol{K}_k^t \right] \frac{\partial \Delta \boldsymbol{U}_k}{\partial x_j} \\
&- \sum_{k=1}^{N} \begin{Bmatrix} \sigma_{PN}^{1-p} \sum_{i=1}^{n} \left[\left(\sigma_{vm,i}^{p-2} \boldsymbol{\sigma}_i^T \boldsymbol{V} \boldsymbol{D}_{ik}^t \boldsymbol{B}_i \boldsymbol{L}_i \right) \left(\boldsymbol{K}_k^t \right)^{-1} \frac{\partial \boldsymbol{K}_k^t}{\partial x_j} \Delta \boldsymbol{U}_k \right] \\ +2 \boldsymbol{\lambda}_k^T \int_{\Omega_i} \boldsymbol{L}_i \boldsymbol{B}_i^T \Delta \boldsymbol{\sigma}_{ik} d\Omega_i \end{Bmatrix}.
\end{aligned} \tag{16}$$

To avoid calculating $\partial \Delta \boldsymbol{U}_k / \partial x_j$, set an adjoint equation:

$$\sigma_{PN}^{1-p} \sum_{i=1}^{n} \left(\sigma_{vm,i}^{p-2} \boldsymbol{\sigma}_i^T \boldsymbol{V} \boldsymbol{D}_{ik}^t \boldsymbol{B}_i \boldsymbol{L}_i \right) - 2 \boldsymbol{\lambda}_k^T \boldsymbol{K}_k^t = \boldsymbol{0}. \tag{17}$$

Take $\boldsymbol{\lambda}_k = 1/2\ \boldsymbol{\mu}_k$, and substitute Eq. (17) into Eq. (16). Equation (16) is transformed into:

$$\frac{\partial f^*(\boldsymbol{x})}{\partial x_j} = -\frac{1}{2} \sum_{k=1}^{N} \left(\boldsymbol{\mu}_{jk} \boldsymbol{k}_{jk}^{t(0)} \Delta \boldsymbol{u}_{jk} + \boldsymbol{\mu}_{jk} \int_{\Omega_j} \boldsymbol{L}_j \boldsymbol{B}_j^T \Delta \boldsymbol{\sigma}_{jk} d\Omega_j \right), \tag{18}$$

where $\boldsymbol{k}_{jk}^t = x_j \int \boldsymbol{B}_j^T \boldsymbol{D}_k \boldsymbol{B}_j d\Omega_j$ is the tangent stiffness matrix of the element j participating in the calculation at the k-th load increment step. $\boldsymbol{k}_{jk}^{t(0)} = \int \boldsymbol{B}_j^T \boldsymbol{D}_k \boldsymbol{B}_j d\Omega_j$ is the tangent stiffness matrix of the j-th element at the k-th load increment step.

To maintain the same monotonicity of increase and decrease in sensitivity numbers as the traditional BESO method, an anti-sign factor denoted as $-x_i$ is introduced into Eq. (18), resulting in the original sensitivity expression for each element.

$$\alpha_i^{(0)} = \frac{1}{2} x_i \sum_{k=1}^{N} \left(\boldsymbol{\mu}_{ik} \boldsymbol{k}_{jk}^{t(0)} \Delta \boldsymbol{u}_{jk} + \boldsymbol{\mu}_{ik} \int_{\Omega_j} \boldsymbol{L}_i^T \boldsymbol{B}_i \Delta \boldsymbol{\sigma}_{ik} d\Omega_i \right) \tag{19}$$

To mitigate numerical instabilities in topology optimization (e.g., mesh dependency and checkerboarding), element sensitivities are filtered as follows in Eq. (20):

$$\alpha_i = \frac{\sum_{j=1}^{n} \omega_{ij}^{sen} \alpha_j^{(0)}}{\sum_{j=1}^{n} \omega_{ij}^{sen}}, \tag{20}$$

where ω_{ij}^{sen} is the linear weight factor, calculated as follows:

$$\omega_{ij}^{sen} = \max\left\{0, r_{sen} - \Delta(i,j)\right\}, \tag{21}$$

where r_{sen} is the sensitivity filter radius, typically chosen as 2~3 times the length of the element [18] to ensure the potential restoration of deleted elements. $\Delta(i,j)$ represents the element center-to-center distance between the i-th and the j-th elements.

Simultaneously, the filtered sensitivity undergoes an averaging process with its historical information to improve the optimization procedure's stability. The filtered sensitivity is averaged with the historical information from the two design iterations [37] to add an extra layer of filtration:

$$\alpha_i^{(l)} \leftarrow \frac{\alpha_i^{(l)} + \alpha_i^{(l-1)} + \alpha_i^{(l-2)}}{3} \quad \text{for } l > 2, \tag{22}$$

where (l) denotes the number of design iterations.

Then, by utilizing the doubly filtered sensitivity numbers, the algorithm executes the design variable update operation as follows:

$$x_i^{(l+1)} = \begin{cases} 0 & \text{if } \alpha_i \le \alpha_{del}^{th} \text{ and } x_i^{(l)} = 1 \\ 1 & \text{if } \alpha_i \ge \alpha_{add}^{th} \text{ and } x_i^{(l)} = 0 \\ x_i^{(l)} & \text{others} \end{cases}, \tag{23}$$

where α_{del}^{th} and α_{add}^{th} represent the upper and lower thresholds for sensitivity numbers, determined based on the desired number of element removals and additions corresponding to the volume for the current iteration [18]. To enhance the stability and robustness of the method, a filtering operation is applied to the design variables [38]:

$$x_i = \frac{\sum_{j=1}^{n} \omega_{ij}^{den} x_j}{\sum_{j=1}^{n} \omega_{ij}^{den}}, \tag{24}$$

where ω_{ij}^{den} is the linear weight factor, calculated as follows:

$$\omega_{ij}^{den} = \max\left\{0,\ r_{den} - \Delta(i,j)\right\}, \tag{25}$$

where r_{den} is the filter radius for design variables.

Following Eq. (23), it is necessary to perform an additional design variable update operation [18] to ensure that the topology structure conforms to a well-defined discrete nature since the design variable ranges from 0 to 1.

When reaching the target volume, to avoid getting trapped in a local optimum and to find the global optimal solution as much as possible, while keeping the volume ratio essentially unchanged, continue iterating for a finite number of steps until the difference in the objective function δ satisfies the following condition [39]:

$$\delta = \frac{\left| \sum_{k=1}^{5} \left[(\sigma_{PN})^{iter-4-k} \right] - \sum_{k=1}^{5} \left[(\sigma_{PN})^{iter+1-k} \right] \right|}{\left| \sum_{k=1}^{5} (\sigma_{PN})^{iter+1-k} \right|} < 0.001, \tag{26}$$

where *iter* represents the current iteration number. After reaching the target volume ratio, extract the objective function values for ten consecutive generations, and calculate the rate of change between the sum of the objective function values of the last five generations and that of the first five generations. If this rate of change does not exceed the limit value (unified as 0.001 in this study), the convergence criterion is considered satisfied. In this case, the generation with the minimum objective function value is selected as the optimal topology output. If the criterion is not met, continue iterating. If the upper limit of iterations (unified as 20 in this study) is reached, select the generation

with the minimum objective function value among these 20 generations as the optimal topology output.

3 Optimization process and numerical examples

3.1 Optimization process

The processes for the stress-based BESO method are as follows:

1. Define the initial design domain, partition the finite-element mesh and specify boundary conditions;
2. Define the optimization control parameters for the BESO method, which includes the volume constraint V^*, the evolutionary rate cer, and the maximum admission ratio car;
3. Determine the total number of iterations required for the optimization process based on the target volume and the evolutionary rate, and then loop over the design iterations as follows:
   - Calculate the target volume for the current iteration;
   - Perform FEA on the structure of the current iteration;
   - Assess whether the convergence conditions for the imbalanced equation are satisfied. If they are met, proceed to the next step; if not, reevaluate the unbalanced force;
   - Evaluate sensitivity numbers according to Eq. (19);
   - Filter and average the sensitivity numbers using Eqs. (20) and (22);
   - Update and filter design variables;
   - Perform removal and restoration on elements;
   - Determine whether the volume constraints are satisfied. If they are met, exit the process; if not, return to the first step of this dotted listing.
4. Continue iterating for n cycles, with n being a preset value based on experience, typically taken as 10;
5. Calculate the sum of the objective function values from the first $n/2$ iterations and the sum from the last $n/2$ iterations, and then calculate the difference between them;
6. Assess whether the difference is below the predetermined threshold. If it does, proceed to the next step; if not, continue iterating for an additional n cycles;
7. Identify the topology with the lowest peak stress from the final n or $2n$ iterations, and output it as the topological solution.

The specific optimization process is shown in Fig. 1.

3.2 Numerical examples of 2D structures

3.2.1 Example overview

The design domain and basic parameters of an irregular concrete beam [40] are illustrated in Fig. 2. Reinforced concrete is modeled as a composite material with a Young's modulus of 3.25×10^4 N/mm^2 and a Poisson's ratio of 0.3. The structure is discretized into quadrilateral elements under the plane stress assumption, with an element side length of $h_e = 5$ mm. A vertical load of $F = 20$ kN is applied to the beam, evenly distributed across 10 elements over 10 load steps to mitigate stress concentration. The target volume fraction is set to 30%, and the reference stress σ_{s0} is

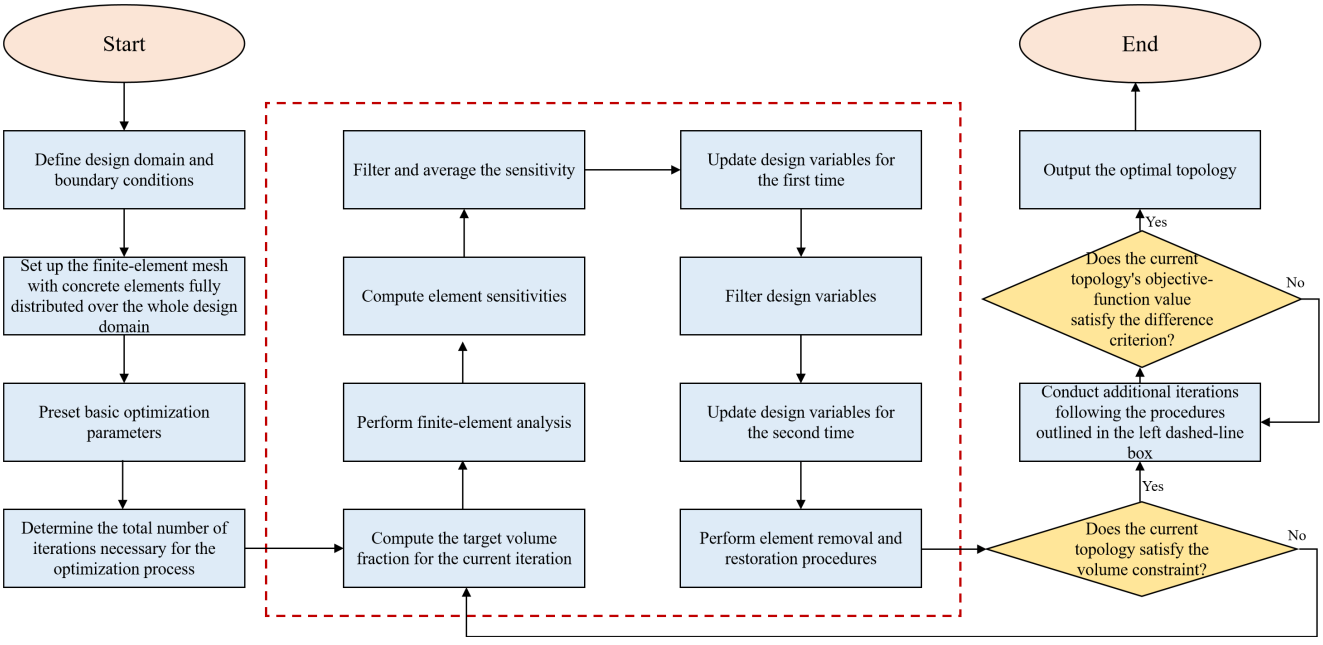

Fig. 1 Flow chart of the method

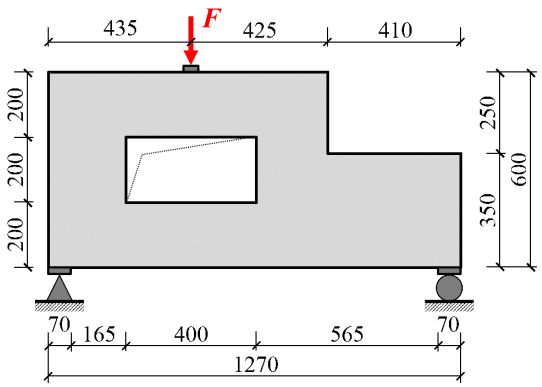

Fig. 2 Illustration of the irregular beam problem [40] (units: mm)

defined as 4.0 N/mm^2. The evolutionary rate c_{er} and maximum material restoration ratio c_{ar} are set to 2% and 0.5%, respectively, for each iteration. The sensitivity filter radius r_{sen} and design variable filter radius r_{den} are set to 3 and 6 times the element side length, respectively. The base number of convergence iterations, denoted as n, is defined as 10. All finite element analysis and topology optimization iterative calculations in this study were implemented using MATLAB software [41].

3.2.2 Material constitutive

A nonlinear constitutive relationship incorporating strain hardening [37] is adopted, as illustrated in Fig. 3.

3.2.3 Optimization results and analysis

When the p-value is set to 6, the optimization process of the objective function is shown in Fig. 4.

As shown in Fig. 4, the optimization process can be divided into three distinct stages:

1. The first stage, the preliminary design phase, is characterized by a relatively constant difference between the number of removed and reinstated elements, alongside a gradual reduction in topological element count. For example, in early iterations, the primarily removed elements were located at the beam's two corners and the lower abdomen region. Guided by Saint-Venant's principle in elastic mechanics and the stress distribution of the bending component's cross-section, these areas are identified as experiencing near-zero stress. By the stage's conclusion (e.g., the 43rd iteration in this example), the topology had formed the beam's primary skeletal configuration.
2. The second stage, the evolutionary attempt phase, involves trial-and-error topological evolution with a relatively stable difference between deleted and restored element counts. This leads to objective function oscillations due to alternating removal and restoration of specific elements. For example, in the 59th iteration, the initial removal of specific elements in two void regions caused equivalent stress at those locations to peak, significantly exceeding the previous iteration's peak stress. However, these elements were later reinstated, and the void-region elements restored, reducing the topological peak stress. This dynamic process induced substantial objective function fluctuations. The topology stabilized when the target volume fraction was achieved (e.g., the 61st iteration in this example), with a relatively well-defined shape.
3. The third stage, after achieving the target volume fraction, is the fine-tuning optimization phase. In this stage, the count of deleted and restored elements in each iteration is balanced. The primary strategy entails performing removal and restoration of individual elements in localized regions to refine topological details. The ultimate goal is to identify the optimal solution with the minimum peak stress. The 68th iteration topology, featuring the minimum peak stress, was selected as the optimal solution for output.

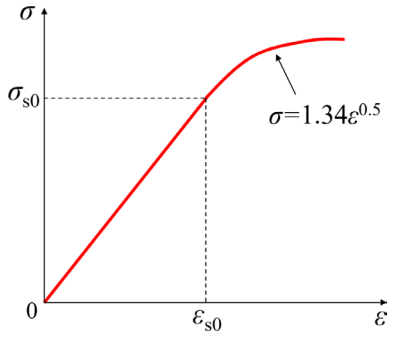

Fig. 3 Material constitutive [37]

As shown in Fig. 4, both the peak von Mises stress (σ_{max}) and the objective function value (σ_{PN}) in the 8th iteration topology are lower than those in the 1st iteration (initial topology). This indicates that the early optimization phase reduces structural volume while slightly decreasing peak stress, primarily by removing near-zero-stress elements. However, as iterations proceed, the algorithm continuously removes low-stress elements, reducing the number of elements in the topology. This inevitably increases the overall stress levels, causing the objective function value to rise. The core optimization goal remains minimizing peak von Mises stress under volume constraints, which essentially requires slowing the growth rate of the objective function as elements are removed. Thus, the observed increase in the objective function value is consistent with the fundamental optimization objective.

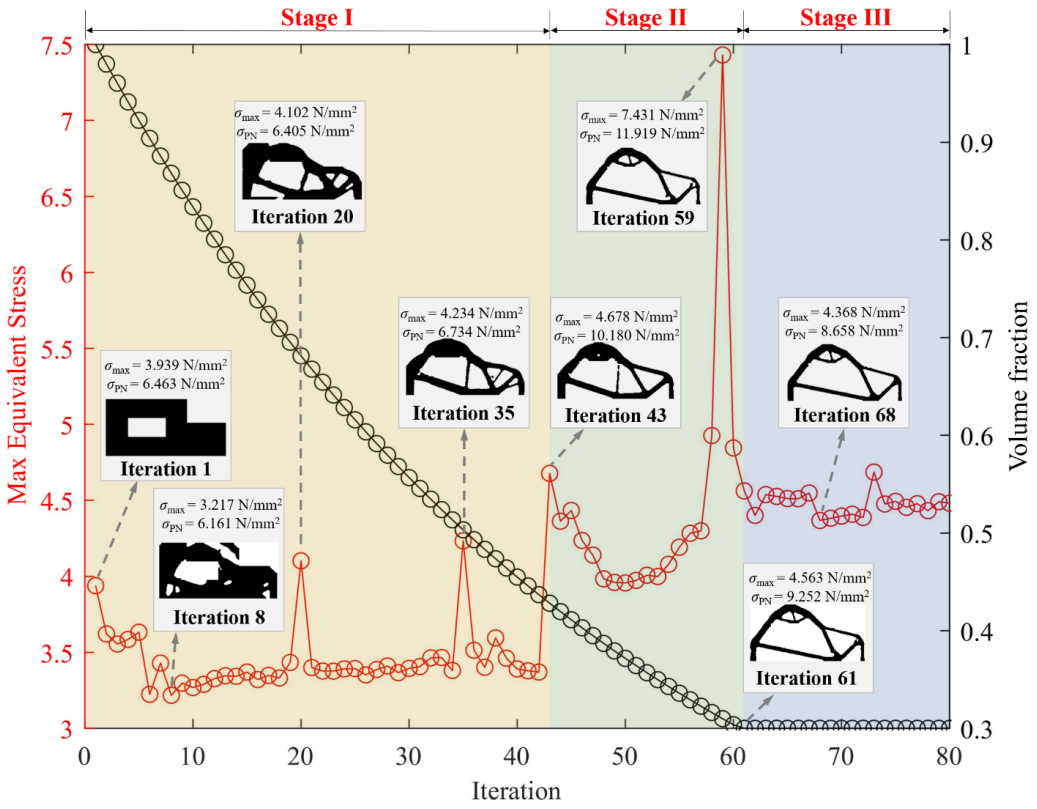

Fig. 4 Optimization process step curves ($p = 6$)

Throughout the optimization process, peak stress exhibits fluctuations. This arises because the p-norm aggregation function – the objective function – can become ill-conditioned at high p-values, while a limited p-value introduces discrepancies between the objective function and its p-norm approximation. Despite the substantial reduction in target volume fraction, peak stress within the structure remains effectively managed, demonstrating the optimization process's effectiveness. The detailed effects of different p-values on optimization will be further investigated in Section 4.

4 Typical L-shaped beam calculation example

To verify the proposed method's applicability to traditional structure optimization, a typical L-shaped beam [42] is selected to analyze. The material is a Young's modulus of 1 N/mm^2 and a Poisson's ratio of 0.3. A vertical load of $F = 16$ N applied to the beam, divided into 16 load steps. Optimization parameters include an evolutionary rate $c_{er} = 1\%$, maximum material restoration ratio $c_{ar} = 0.05\%$, sensitivity filter radius $r_{sen} = 2\ h_e$, design variable filter radius $r_{den} = 6\ h_e$, target volume fraction of 40%, and reference stress $\sigma_{s0} = 6.0$ N/mm^2, where h_e denotes the element side length. Table 1 presents the optimal solutions and stress results for different p-values.

From Table 1, it can be seen that as the p-value increases, both the peak stress and p-norm stress decrease, and the corners are smoothed, avoiding the stress concentration. Therefore, the optimization method proposed in this paper is also applicable to typical L-shaped structures.

Table 1 Comparison of peak stress results under different p-values

	$p = 2$	$p = 4$	$p = 6$	$p = 8$
Topology solutions	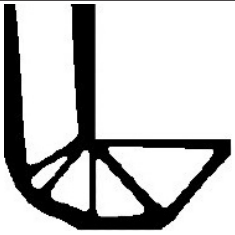	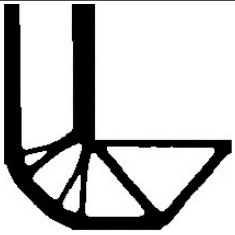	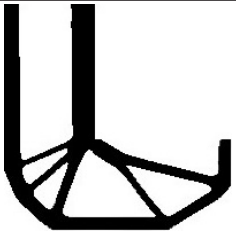	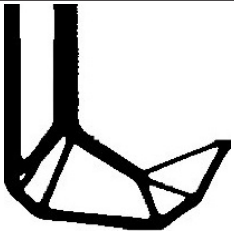
σ_{max} (N/mm^2)	7.38	7.26	6.35	6.02
σ_{PN} (N/mm^2)	227.53	23.44	11.89	10.36

5 Comparison of stress-based BESO methods

Xia et al. [18] introduced a stress-based BESO method using linear-elastic structural analysis, which shares the same objective as the present study's method. Their study validated the method using a planar cantilever beam structure (shown in Fig. 5). For comparative analysis, Section 5 employs the same example to conduct stress-based BESO with both methods. A vertical load of F = 5 N is applied to the structure, evenly distributed across 9 elements over 15 load steps to mitigate stress concentration. Analysis and optimization parameters match those of the linear-elastic BESO method in Xia et al. [18]; unspecified parameters follow those used in the planar irregular beam example (Section 3.2.1): Material Young's modulus is 1.0 N/mm^2, reference stress σ_{s0} = 0.9 N/mm^2, and the structure is discretized into quadrilateral elements under plane stress assumption with an element side length h_e = 1 mm. The sensitivity filter radius rsen and design variable filter radius rden are set to 2 h_e and 5 h_e respectively, with a target volume fraction of 50%. The optimization results are presented in Table 2.

Regarding computational cost, the incremental nonlinear BESO method required 221, 196, and 249 min for optimization under different p-values, substantially higher than the 15–17 min of the linear-elastic method. This increase stems primarily from the iterative equilibrium solutions in each nonlinear finite element analysis and the adjoint-based sensitivity accumulation across all load steps. Although the computational cost rises by approximately one order of magnitude, the peak stress is reduced by 4.85–7.69%, demonstrating the method's advantage when higher optimization quality is desired. For large-scale structures, efficiency can be improved by reducing the number of load steps or employing parallel computing, thereby balancing accuracy and computational resources.

Compared to the linear-elastic BESO method in Xia et al. [18], the incremental nonlinear BESO method presents two distinct advantages:

1. First, smaller p-norm values yield more favorable and applicable solutions. For example, when p = 6, the incremental nonlinear BESO method yields an optimal topology with a peak stress σ_{max} = 0.98 N/mm^2. With stress fields recalculated *via* incremental nonlinear analysis, the linear-elastic method of Xia et al. [18] results in a peak stress of 1.03 N/mm^2. With the p-values of 2 and 4, the incremental nonlinear method aligns more closely with optimization objectives, demonstrating superior optimality.
2. Second, the incremental nonlinear BESO method tends to be stabler. For example, when p = 8, the linear-elastic method from Xia et al. [18] fails to converge. In contrast, the incremental nonlinear method consistently produces a stable topology solution, though its peak stress σ_{max} is higher than the case of p = 6.

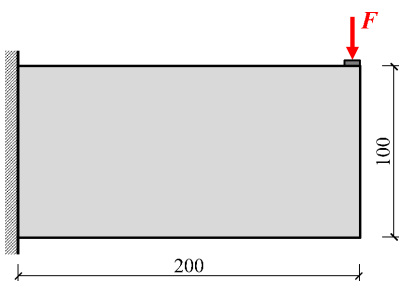

Fig. 5 Illustration of the planar cantilever beam problem [18] (units: mm)

Thus, for structures with strong nonlinear materials, the stress-based BESO method incorporating incremental nonlinear analysis yields more robust topology solutions than linear-elastic-based approaches. It is because, under high loads where elements move to the elastoplastic stage, linear elastic analysis overestimates stresses in these elements compared to their actual elastoplastic stress values. Since element sensitivity depends on stress, topology optimization using these overestimated stress can distort the relative sensitivity magnitudes between elements. More critically, during sensitivity filtering, pseudo-information from elevated linear-elastic stresses can corrupt sensitivity values of neighboring elements within the filter radius, distorting sensitivity rankings and compromising optimization outcomes. While nonlinear analysis in Table 2 requires approximately 4 h – compared to less than 1 h for linear analysis – it reduces maximum stress by 5–8% relative to linear-elastic results.

6 Numerical examples of 3D structures

The 3D cantilever beam from Xia et al. [18], with characteristic dimensions, is depicted in Fig. 6 (a). A vertical load of F = 25 N is applied to the beam's free end. The load is uniformly distributed over 16 elements to mitigate stress concentration and applied in 2 load steps in nonlinear analysis. Analysis and optimization parameters match those in Xia et al. [18]; unspecified parameters follow the planar structure example in Section 3.2. Material Young's modulus is 1.0 N/mm^2, and reference stress σ_{s0} = 1.0 N/mm^2. The structure is discretized using eight-node cubic elements with an element side length h_e = 1 mm. Sensitivity filter radius rsen and design variable filter radius rden are both set to twice the element side length. With p = 6, optimization yields the optimal topology at the 70th iteration (σ_{max} = 1.572 N/mm^2, σ_{PN} = 3.866 N/mm^2), as illustrated in Fig. 6 (b).

Table 2 Comparison of the two stress-based BESO methods

Optimization method		*p*-value		
		2	4	6
The BESO method with structural linear-elastic analysis [18]	Topology solutions			
	σ_{max} (N/mm^2)	1.31	1.14	1.03
	σ_{PN} (N/mm^2)	39.07	4.26	2.14
	Computational cost (min)	15	17	15
The BESO method with incremental nonlinear structural analysis	Topology solutions			
	σ_{max} (N/mm^2)	1.21	1.08	0.98
	σ_{PN} (N/mm^2)	39.09	4.29	2.23
	Computational cost (min)	221	196	249

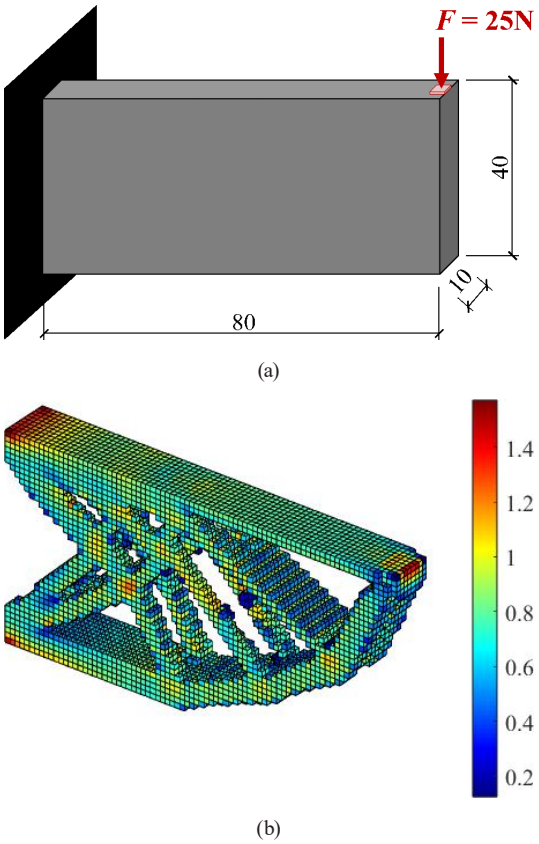

Fig. 6 3D cantilever beam problem: (a) design domain [18] (units: mm); (b) topology solution and its equivalent stress distribution (units: N/mm^2)

As shown in Fig. 6 (b), the stress-based BESO method is effectively applicable to 3D structures. This method effectively controls peak stress growth while ensuring consistent material reduction, yielding well-defined 3D optimal topologies. It is important to note that all optimizations were performed on a specific hardware configuration: an Intel® Core™ i9-9900K CPU @ 3.60GHz (quad-core), 16GB Zhiqi DDR4 2133MHz RAM, and an NVIDIA GeForce GTX 1650 graphics card. Under this configuration, the full optimization of the 3D cantilever beam requires approximately 11 h. A similar optimization of a planar cantilever beam in Section 7 takes approximately 2.5 h. Notably, the 3D optimization time is 4.4 times that of the 2D example. This discrepancy stems from two key factors:

1. First, the 3D model contains 32,000 elements – 1.6 times that in the planar model – leading to higher computational demands.
2. Second, 3D structures use eight-node cubic elements – with twice as many nodes per element as planar four-node square elements – making displacement calculations inherently more time-consuming.

Additionally, the number of load increment steps seriously influences calculation time. Increasing load steps in the 3D example from 2 to 10 (matching the planar example) would further widen the computational efficiency gap. Thus, planar structures are recommended for optimization when spatial characteristics are not critical.

7 The effect of *p*-value

Using the planar irregular beam structure from Section 3.2.1 and keeping all other parameters constant, BESO optimization for peak stress is performed with stress norms $p = 2$, 4, and 6, respectively. The stress results of the obtained optimal topology solutions are presented in Table 3.

Table 3 clearly shows the relationship between the *p*-value and peak stress σ_{max}. As the *p*-value increases,

Table 3 The stress-based BESO method results with different *p*-values

Results	*p*-value		
	2	4	6
Topology solutions	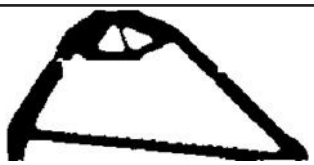		
σ_{max} (N/mm^2)	4.87	4.56	4.37
σ_{PN} (N/mm^2)	142.00	16.96	8.66

σ_{max} decreases monotonically, leading to a more uniform stress distribution and a significant reduction in the objective function σ_{PN}. When the *p*-value exceeds 6, Optimization convergence can be impeded by further increases, potentially preventing attainment of the desired topology. Excessively low *p*-values result in higher objective function values, signaling sub-optimal topology solutions, while excessively high *p*-values ill-condition the p-norm problem, precluding acquisition of the optimal topology. This stems from the *p*-norm approaching the true objective function as *p*-value increases. However, high *p*-values induce optimization divergence for two key reasons:

1. First, large element sensitivity disparities emerge, which sensitivity and design variable filtering can mitigate but not eliminate;
2. Second, using stress – a local parameter – for optimization introduces numerical instability, as individual element state changes can drastically alter structural stress distributions, undermining optimization stability. Thus, a *p*-value in the range of 4–6 is recommended for optimal performance.

Additionally, with all other conditions held constant, the load was evenly distributed between two elements for FEA and subsequent optimization. Results show that peak stress σ_{max} increases monotonically as the *p*-value rises. This stems from severe stress concentration at the load application point, where peak stress consistently occurs, thereby diminishing the optimization effect. Thus, when applying the proposed optimization method, moderately dispersing load concentration and increasing the load-bearing area is necessary to mitigate such issues.

8 Conclusions

The stress-based BESO method incorporating incremental nonlinear structural analysis aims to minimize structural peak stress by approximating it using the *p*-norm function, with sensitivity derived *via* the adjoint method. Example studies validate the method's effectiveness and applicability, leading to the following key conclusions:

1. When using the *p*-norm function to approximate structural peak stress, increasing the *p*-value significantly reduces global stress levels and promotes a more uniform overall stress distribution.
2. Maintaining a *p*-value of at least 4 ensures topology solutions closely align with predefined optimization objectives. Higher *p*-values yield more direct force transmission and clearer load path visualization. However, *p*-values exceeding 8 risk numerical instability and convergence issues. Therefore, a *p*-value between 4 and 6 is recommended for robust stress-based BESO optimization.
3. For structures with strongly nonlinear materials, incremental nonlinear analysis delivers more accurate stresses than linear-elastic methods. Since element initial sensitivity is stress-dependent, this produces more accurate filtered sensitivity rankings–enabling rational element removal/restoration during topology optimization and yielding more stable optimal solutions.

Acknowledgment

Funding: this work was supported by the National Natural Science Foundation of China (Grant No. 52478172); and the Natural Science Foundation of Hunan Province, China (Grant No. 2024JJ9062).

References

[1] Bendsøe, M. P., Kikuchi, N. "Generating optimal topologies in structural design using a homogenization method", Computer Methods in Applied Mechanics and Engineering, 71(2), pp. 197–224, 1988. https://doi.org/10.1016/0045-7825(88)90086-2

[2] Jeong, S. H., Park, S. H., Choi, D.-H., Yoon, G. H. "Topology optimization considering static failure theories for ductile and brittle materials", Computers & Structures, 110–111, pp. 116–132, 2012. https://doi.org/10.1016/j.compstruc.2012.07.007

[3] Zhang, H., Chen, Y., Chen, H., Xiao, Q., Xu, W. "Experimental investigation and simulation on load-transfer paths in optimally designed RC deep beams", Engineering Structures, 278, 115469, 2023. https://doi.org/10.1016/j.engstruct.2022.115469

[4] Mekki, B. S., Langer, J., Lynch, S. "Genetic algorithm based topology optimization of heat exchanger fins used in aerospace applications", International Journal of Heat and Mass Transfer, 170, 121002, 2021. https://doi.org/10.1016/j.ijheatmasstransfer.2021.121002

[5] Lu, F., Long, K., Zhang, C., Zhang, J., Tao, T. "A novel design of the offshore wind turbine tripod structure using topology optimization methodology", Ocean Engineering, 280, 114607, 2023. https://doi.org/10.1016/j.oceaneng.2023.114607

[6] Wang, L., Zhang, H., Zhu, M., Chen, Y. F. "A new Evolutionary Structural Optimization method and application for aided design to reinforced concrete components", Structural and Multidisciplinary Optimization, 62(5), pp. 2599–2613, 2020. https://doi.org/10.1007/s00158-020-02626-z

[7] Zhang, H., Luo, P., Yuan, J., Huang, Y., Liu, J. "Reinforcement layout design for deep beam based on BESO of multi-level reinforcement diameter under discrete model", Structural Engineering and Mechanics, 84(4), pp. 547–560, 2022. https://doi.org/10.12989/sem.2022.84.4.547

[8] Zhang, H., Liu, X., Fang, Z., Yin, B. "An improved GBESO method and application for engineering structures", Structures, 57, 105083, 2023. https://doi.org/10.1016/j.istruc.2023.105083

[9] Li, Z., Shi, T., Xia, Q. "Eliminate localized eigenmodes in level set based topology optimization for the maximization of the first eigenfrequency of vibration", Advances in Engineering Software, 107, pp. 59–70, 2017. https://doi.org/10.1016/j.advengsoft.2016.12.001

[10] Xu, B., Han, Y. S., Zhao, L., Xie, Y. M. "Topology optimization of continuum structures for natural frequencies considering casting constraints", Engineering Optimization, 51(6), pp. 941–960, 2019. https://doi.org/10.1080/0305215X.2018.1506771

[11] Buhl, T., Pedersen, C. B. W., Sigmund, O. "Stiffness design of geometrically nonlinear structures using topology optimization", Structural and Multidisciplinary Optimization, 19(2), pp. 93–104, 2000. https://doi.org/10.1007/s001580050089

[12] Le, C., Norato, J., Bruns, T., Ha, C., Tortorelli, D. "Stress-based topology optimization for continua", Structural and Multidisciplinary Optimization, 41(4), pp. 605–620, 2010. https://doi.org/10.1007/s00158-009-0440-y

[13] Cheng, G. D., Guo, X. "ε-relaxed approach in structural topology optimization", Structural Optimization, 13(4), pp. 258–266, 1997. https://doi.org/10.1007/BF01197454

[14] Luo, Y., Kang, Z. "Topology optimization of continuum structures with Drucker–Prager yield stress constraints", Computers & Structures, 90–91, pp. 65–75, 2012. https://doi.org/10.1016/j.compstruc.2011.10.008

[15] Moon, S. J., Yoon, G. H. "A newly developed *qp*-relaxation method for element connectivity parameterization to achieve stress-based topology optimization for geometrically nonlinear structures", Computer Methods in Applied Mechanics and Engineering, 265, pp. 226–241, 2013. https://doi.org/10.1016/j.cma.2013.07.001

[16] Takezawa, A., Yoon, G. H., Jeong, S. H., Kobashi, M., Kitamura, M. "Structural topology optimization with strength and heat conduction constraints", Computer Methods in Applied Mechanics and Engineering, 276, pp. 341–361, 2014. https://doi.org/10.1016/j.cma.2014.04.003

[17] Yang, X. Y., Xie, Y. M., Steven, G. P., Querin, O. M. "Bidirectional Evolutionary Method for Stiffness Optimization", AIAA Journal, 37(11), pp. 1483–1488, 1999. https://doi.org/10.2514/2.626

[18] Xia, L., Zhang, L., Xia, Q., Shi, T. "Stress-based topology optimization using bi-directional evolutionary structural optimization method", Computer Methods in Applied Mechanics and Engineering, 333, pp. 356–370, 2018. https://doi.org/10.1016/j.cma.2018.01.035

[19] Duysinx, P., Bendsøe, M. P. "Topology optimization of continuum structures with local stress constraints", International Journal for Numerical Methods in Engineering, 43(8), pp. 1453–1478, 1998. https://doi.org/10.1002/(SICI)1097-0207(19981230)43:8<1453::AID-NME480>3.0.CO;2-2

[20] Yang, R. J., Chen, C. J. "Stress-based topology optimization", Structural Optimization, 12(2), pp. 98–105, 1996. https://doi.org/10.1007/BF01196941

[21] Fan, Z., Xia, L., Lai, W., Xia, Q., Shi, T. "Evolutionary topology optimization of continuum structures with stress constraints", Structural and Multidisciplinary Optimization, 59(2), pp. 647–658, 2019. https://doi.org/10.1007/s00158-018-2090-4

[22] Senhora, F. V., Giraldo-Londoño, O., Menezes, I. F. M., Paulino, G. H. "Topology optimization with local stress constraints: a stress aggregation-free approach", Structural and Multidisciplinary Optimization, 62(4), pp. 1639–1668, 2020. https://doi.org/10.1007/s00158-020-02573-9

[23] Han, Y., Xu, B., Wang, Q., Liu, Y., Duan, Z. "Topology optimization of material nonlinear continuum structures under stress constraints", Computer Methods in Applied Mechanics and Engineering, 378, 113731, 2021. https://doi.org/10.1016/j.cma.2021.113731

[24] Movahedi Rad, M., Habashneh, M., Logo, J. "Elasto-Plastic limit analysis of reliability based geometrically nonlinear bi-directional evolutionary topology optimization", Structures, 34, pp. 1720–1733, 2021. https://doi.org/10.1016/j.istruc.2021.08.105

[25] Habashneh, M., Movahedi Rad, M. "Plastic-limit probabilistic structural topology optimization of steel beams", Applied Mathematical Modelling, 128, pp. 347–369, 2024. https://doi.org/10.1016/j.apm.2024.01.029

[26] Izzi, M. I., Catapano, A., Montemurro, M. "Strength and mass optimisation of variable-stiffness composites in the polar parameters space", Structural and Multidisciplinary Optimization, 64(4), pp. 2045–2073, 2021. https://doi.org/10.1007/s00158-021-02963-7

[27] Montemurro, M., Roiné, T. "Strength-based topology optimisation of anisotropic continua in a CAD-compatible framework", Advances in Engineering Software, 189, 103591, 2024. https://doi.org/10.1016/j.advengsoft.2023.103591

[28] Roiné, T., Montemurro, M., Pailhès, J. "Stress-based topology optimization through non-uniform rational basis spline hyper-surfaces", Mechanics of Advanced Materials and Structures, 29(23), pp. 3387–3407, 2022.
https://doi.org/10.1080/15376494.2021.1896822

[29] Ryu, Y. S., Haririan, M., Wu, C. C., Arora, J. S. "Structural design sensitivity analysis of nonlinear response", Computers & Structures, 21(1–2), pp. 245–255, 1985.
https://doi.org/10.1016/0045-7949(85)90247-0

[30] Tsay, J. J., Arora, J. S. "Nonlinear structural design sensivitity analysis for path dependent problems. Part 1: General theory", Computer Methods in Applied Mechanics and Engineering, 81(2), pp. 183–208, 1990.
https://doi.org/10.1016/0045-7825(90)90109-Y

[31] Pedersen, C. B. W. "Crashworthiness design of transient frame structures using topology optimization", Computer Methods in Applied Mechanics and Engineering, 193(6–8), pp. 653–678, 2004.
https://doi.org/10.1016/j.cma.2003.11.001

[32] Boroomand, B., Barekatein, A. R. "On topology optimization of linear and nonlinear plate problems", Structural and Multidisciplinary Optimization, 39(1), pp. 17–27, 2009.
https://doi.org/10.1007/s00158-008-0311-y

[33] Cho, S., Jung, H.-S. "Design sensitivity analysis and topology optimization of displacement-loaded non-linear structures", Computer Methods in Applied Mechanics and Engineering, 192(22–24), pp. 2539–2553, 2003.
https://doi.org/10.1016/S0045-7825(03)00274-3

[34] Huang, X., Xie, Y. M. "Topology optimization of nonlinear structures under displacement loading", Engineering Structures, 30(7), pp. 2057–2068, 2008.
https://doi.org/10.1016/j.engstruct.2008.01.009

[35] Jog, C. S. "A dual algorithm for the topology optimization of non-linear elastic structures", International Journal for Numerical Methods in Engineering, 77(4), pp. 502–517, 2009.
https://doi.org/10.1002/nme.2422

[36] Xia, L., Fritzen, F., Breitkopf, P. "Evolutionary topology optimization of elastoplastic structures", Structural and Multidisciplinary Optimization, 55(2), pp. 569–581, 2017.
https://doi.org/10.1007/s00158-016-1523-1

[37] Xu, B., Han, Y. S., Zhao, L. "Bi-directional evolutionary stress-based topology optimization of material nonlinear structures", Structural and Multidisciplinary Optimization, 63(3), pp. 1287–1305, 2021.
https://doi.org/10.1007/s00158-020-02757-3

[38] Han, Y., Xu, B., Duan, Z., Huang, X. "Stress-based bi-directional evolutionary structural topology optimization considering nonlinear continuum damage", Computer Methods in Applied Mechanics and Engineering, 396, 115086, 2022.
https://doi.org/10.1016/j.cma.2022.115086

[39] Chen, X.-D., Zhang, H.-Z., Kang, Y.-J., Chen, Y. F. "Advancing crack resistance in reinforced concrete: a strain-based topology optimization methodology with material nonlinearity", Structural and Multidisciplinary Optimization, 68(12), 250, 2025.
https://doi.org/10.1007/s00158-025-04197-3

[40] Zhong, J. T., Wang, L., Deng, P., Zhou, M. "A new evaluation procedure for the strut-and-tie models of the disturbed regions of reinforced concrete structures", Engineering Structures, 148, pp. 660–672, 2017.
https://doi.org/10.1016/j.engstruct.2017.07.012

[41] The MathWorks, Inc. "MATLAB, (R2023a (9.14.0))", [computer program] Available at: https://www.mathworks.com [Accessed: 01 December 2025]

[42] Chen, A., Cai, K., Zhao, Z.-L., Zhou, Y., Xia, L., Xie, Y. M. "Controlling the maximum first principal stress in topology optimization", Structural and Multidisciplinary Optimization, 63(1), pp. 327–339, 2021.
https://doi.org/10.1007/s00158-020-02701-5